

Measurement-induced population switching

Michael S. Ferguson ^{1,*}, Leon C. Camenzind ^{2,*†}, Clemens Müller ^{1,3}, Daniel E. F. Biesinger,^{2,4} Christian P. Scheller ²,
Bernd Braunecker ⁵, Dominik M. Zumbühl ² and Oded Zilberberg^{1,6}

¹*Institute for Theoretical Physics, ETH Zurich, 8093 Zurich, Switzerland*

²*Department of Physics, University of Basel, 4056 Basel, Switzerland*

³*IBM Quantum, IBM Research Europe - Zurich, 8803 Rüschlikon, Switzerland*

⁴*Hahn-Schickard, Institute for Information and Microtechnology, Wilhelm-Schickard-Straße 10, 78052 Villingen-Schwenningen, Germany*

⁵*SUPA, School of Physics and Astronomy, University of St Andrews, St Andrews KY16 9SS, United Kingdom*

⁶*Department of Physics, University of Konstanz, D-78464 Konstanz, Germany*



(Received 4 October 2022; accepted 21 February 2023; published 14 April 2023)

Quantum information processing is a key technology in the ongoing second quantum revolution, with a wide variety of hardware platforms competing toward its realization. An indispensable component of such hardware is a measurement device, i.e., a quantum detector that is used to determine the outcome of a computation. The act of measurement in quantum mechanics, however, is naturally invasive as the measurement apparatus becomes entangled with the system that it observes. This always leads to a disturbance in the observed system, a phenomenon called quantum measurement backaction, which should solely lead to the collapse of the quantum wave function and the physical realization of the measurement postulate of quantum mechanics. Here we demonstrate that backaction can fundamentally change the quantum system through the detection process. For quantum information processing, this means that the readout alters the system in such a way that a faulty measurement outcome is obtained. Specifically, we report a backaction-induced population switching, where the bare presence of weak, nonprojective measurements by an adjacent charge sensor inverts the electronic charge configuration of a semiconductor double quantum dot system. The transition region grows with measurement strength and is suppressed by temperature, in excellent agreement with our coherent quantum backaction model. Our result exposes backaction channels that appear at the interplay between the detector and the system environments, and opens new avenues for controlling and mitigating backaction effects in future quantum technologies.

DOI: [10.1103/PhysRevResearch.5.023028](https://doi.org/10.1103/PhysRevResearch.5.023028)

I. INTRODUCTION

Quantum information processing relies on coherently controlling and coupling individual quantum bits (qubits) [1]. Examples of qubit hardware include electron and nuclear spins in quantum dots [2–5], localized charge states [6], superconducting devices [7,8], internal states of trapped ions [9,10], and even Majorana modes in topological materials [11], each system bearing its own advantages and challenges. Regardless of the specific implementation, sensitive detectors are required to extract information about the system under investigation [1,12].

A quantum detector couples to the system it measures such that their respective quantum states become correlated during the measurement process. In turn, reading out the state of the detector collapses the system toward the outcome of the

measurement, in a process known as backaction [12,13]. On a theoretical level, such a detection process of a quantum state $|\psi\rangle$ relies on the measurement postulate, where a quantum mechanical operator \hat{A} is applied onto the state $\hat{A}|\psi\rangle = \sum_i a_i \langle a_i|\psi\rangle |a_i\rangle$ and collapses it to one of its eigenstates with probability $|\langle a_i|\psi\rangle|^2$ when read out.

The physical realization of the measurement postulate, however, requires a detector device that coherently couples to the quantum system over some time period, e.g., using the von Neumann Hamiltonian $\lambda(t)\hat{X}\hat{A}$, with $\lambda(t)$ the time-dependent coupling rate and \hat{X} the coordinate of the detector [12,14]. Reading out the detector coordinate collapses the state $|\psi\rangle$, whereas depending on λ weak or strong backaction manifests, leading in the latter case to the required realization of the measurement postulate. Alternatively, repeated weak measurements also lead to the required goal via so-called continuous measurements [15,16]. These are commonly realized with transport devices where impinging particles perform individual weak measurements, and the flux rate controls the overall measurement strength [17–23].

Regardless of the realization, an ideal detector operates close to the quantum limit [15,16,24], namely, close to where the backaction it imparts is equal to the rate of information gain about the system's state. Yet, as detector realizations involve coherent coupling between impinging particles and the

*These two authors contributed equally to this work.

†Present address: Center for Emergent Matter Science, RIKEN, 2-1 Hirosawa, Wako-shi, Saitama 351-0198, Japan

Published by the American Physical Society under the terms of the [Creative Commons Attribution 4.0 International](https://creativecommons.org/licenses/by/4.0/) license. Further distribution of this work must maintain attribution to the author(s) and the published article's title, journal citation, and DOI.

quantum system, the combined out-of-equilibrium dynamics of the system-detector evolution is an active field of research, which touches upon the foundations of quantum mechanics. Its broad set of achievements include weak values [25], quantum feedback circuits [16,26], high-precision amplifiers [27], quantum state discrimination [28] and stabilization [16], as well as detector-assisted transport [24,29–31]. The latter implies that quantum systems, which are coupled to particle reservoirs, always experience additional many-body energy-exchange channels of backaction beyond those considered in an ideal detector.

Quantum detectors can be alternatively thought of as out-of-equilibrium environments whose internal dynamics depends on the measured system. As a result, a plethora of backaction channels manifests beyond the ideal quantum detector description [17–24,29,32–36]. Indeed, even standard dissipative environments can fundamentally influence quantum many-body systems and their steady states in often counterintuitive ways [37,38]. Correspondingly, the environment can even trigger abrupt changes in the system’s observable properties; i.e., it can induce phase transitions or sharp crossovers [39–43]. As a result, new universality classes [44] and novel topological effects [45,46] emerge in driven-dissipative systems.

In this work, we report on a measurement-induced many-body population switching. We observe this transition in an open many-body quantum system, i.e., a double quantum dot (DD) where the two dots are coupled to each other only capacitively, and each dot is tunnel-coupled to a lead. An adjacent charge sensor dot (CSD) measures the charge state of the DD. The DD exhibits different phases that are characterized by the charge configuration on the quantum dots. In the absence of the detector, these phases are determined by the ground-state energetics of the DD with the leads supplying the charges. We observe that the detector imparts backaction that induces a distinct change in the observed charge configuration. Specifically, we observe that the system now preferentially populates an energetically high-lying state, in close analogy to theoretical predictions for population switching in related systems [47]. We systematically analyze the dependence on measurement strength and temperature of this transition, and develop a concise theory that reproduces the features of the measured data. The backaction-induced population switch highlights the extreme sensitivity of quantum systems to out-of-equilibrium fluctuations: for a qubit fully in state $|0\rangle$ this would correspond to a change into state $|1\rangle$ by the measurement backaction.

II. EXPERIMENT

We perform our experiments on a gate-defined lateral GaAs device [35] with an electron temperature $T_{el} \approx 65$ mK at the base temperature of our dilution refrigerator. By applying voltages to the gate electrodes of our device, we locally deplete the underlying two-dimensional electron gas to form a DD (mint) adjacent to a CSD (pink), as shown in the inset of Fig. 1(a). These gate electrodes are also used to control the tunnel couplings in the system. Each single dot in the DD is tunnel-coupled to a separate lead on each side, both with tunneling rate $\Gamma_{DD} \sim 100$ kHz. Additionally, Coulomb repulsion between the dots (mutual charging energy) $U \approx 215$ μ eV

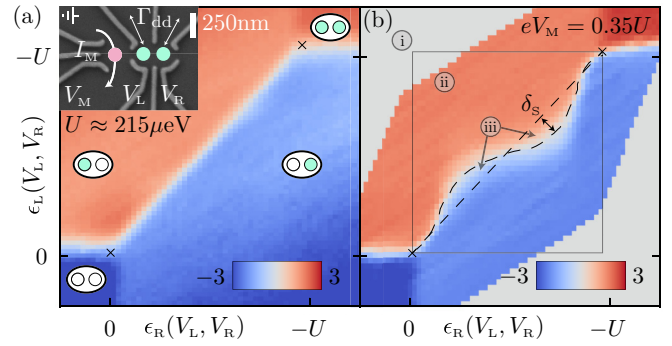


FIG. 1. Charge stability of a double dot with and without the effects of measurement backaction. (a) DD backaction imbalance as a function of the dot energies ϵ_L and ϵ_R for the case of negligible backaction. Since measuring at very low bias is very noisy, we measure at a larger measurement bias $V_M = 150$ μ eV and turn on the interdot tunneling to mimic the canonical DD charge stability diagram as obtained in the absence of backaction. Full (mint) and empty (white) circles illustrate the ground state in each region of the observed charge stability map. Inset: Scanning electron micrograph of the device. The population of the DD (mint circles) is monitored by a nearby charge sensor dot (pink circle). (b) Same as (a), using a measurement bias $V_M = 75$ μ eV ($0.35U/e$). The interdot tunneling is completely suppressed such that the effects of backaction become apparent in a distortion of the boundary between left and right occupied states. Marked regions (i), (ii), (iii) are governed by different physical mechanisms (see details in the text). Both measurements (a) and (b) were performed at an electronic temperature $T \approx 65$ mK.

imposes an energy penalty on the doubly occupied states and thus acts to diminish the occupancy of the DD. Crucially to this work, interdot tunneling is negligibly small in the DD (see Appendix A for further experimental details). The plunger gate voltages V_L and V_R are used to tune the left- and right-dot energies ϵ_L and ϵ_R . These in turn tune the DD populations (N_L, N_R) , i.e., the number of electrons of the left and right dots, respectively. We perform our experiment in a parameter region where only four distinct charge states of the DD are relevant, i.e., empty (0,0), left occupied (1,0), right occupied (0,1), or doubly occupied (1,1). In the absence of interdot tunneling, the metastability in the canonical charge stability diagram [35] becomes measurable with the CSD and, simultaneously, all transitions in the DD necessarily involve the reservoirs which serves an important role in the following. The corresponding charge stability map displays sharp crossovers between distinct DD population configurations; see Fig. 1(a).

The population states (N_L, N_R) have probabilities $P_{(N_L, N_R)}$ to be observed. The detector has a bandwidth of 15 kHz which allows us to measure this probability distribution by real-time monitoring of its tunneling current I_M in response to an applied bias voltage V_M across the CSD [35]. This enables direct observation of the population imbalance $\Delta = 2P_{(1,0)} - 2P_{(0,1)} + 3P_{(1,1)} - 3P_{(0,0)}$ (see Appendix A), which serves as an order parameter for our system. Microscopically, each charge tunneling event through the detector realizes a weak measurement kick onto the system through the DD-CSD capacitive interactions. The interplay of such a flux of impinging detector electrons with the double dot and its reservoirs is inherently an out-of-equilibrium many-body effect. Varying

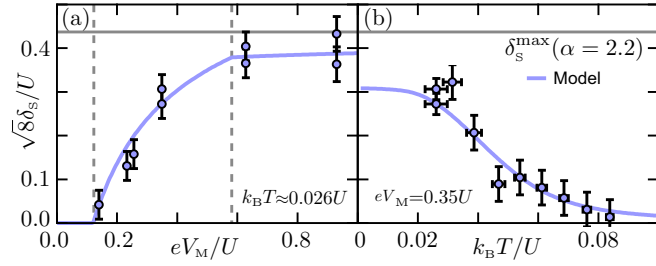


FIG. 2. Scaling of δ_s . Measured maximal deviation δ_s (circles) as a function of (a) the measurement bias voltage V_M at $k_B T/U = 0.026$ ($T = 65$ mK) and (b) temperature T at $eV_M/U = 0.35$ ($eV_M = 75$ μ eV). Error bars include the uncertainty in determination of the charge-degeneracy curve at $\Delta = 0$ and the uncertainty in the relationship between the fridge temperature and electronic temperature. The theoretical model (cf. Fig. 3), with backaction-induced Lorentzian broadening, reproduces the observed temperature and measurement bias dependence of the effect. The horizontal solid line indicates the maximal possible deviation δ_s predicted by our model for $\alpha = 2.2$, while in the infinite- α limit the saturation is limited by the mutual repulsion and a geometric factor $\delta_s^{\max}(\alpha \rightarrow \infty) = U/\sqrt{8}$. Vertical dashed lines mark points that characterize the two fit parameters χ and ξ of our model.

V_M modifies the current through the detector, thus adjusting the strength of the population measurement [15, 16, 30, 31]. Applying a small bias voltage, $V_M \ll U/e$, results in a conventional charge stability diagram, similar to the one shown in Fig. 1(a), where backaction has no clear effect.

We increase the measurement strength by increasing the bias voltage (to $V_M = 0.35U/e$), and observe a qualitative change in the measured charge stability diagram; see Fig. 1(b). The diagonal *equilibrium phase boundary* that separates the (1,0) and (0,1) states transforms into an S shape, with maximal deviation δ_s from the diagonal. In the area enclosed between the S and the equilibrium phase boundary [region (iii) in Fig. 1(b)], the population of the DD is switched; i.e., a high-energy state is preferentially occupied.

We systematically study the size of the population-switching area as a function of applied measurement voltage V_M and electronic temperature T ; see Fig. 2. At low temperature, we find that the S shape grows, and finally saturates with the bias voltage V_M . In contrast, an increase in temperature washes out the effect. We conclude that at low temperatures and large bias, backaction of the detector on the DD dominates the behavior of the DD. This is the main result of this work, and highlights how sensitive the stationary state of a quantum system can be on the measurement strength. Specifically, the quantum measurement induces a population switch in the state of the DD and its leads. As the DD is coupled to large leads that absorb and emit particles and there is no interdot tunneling, the switch necessitates particle and energy exchange with the leads [47]. Furthermore, we extract the width of the transition in the charge stability diagram. We observe that even though the amplitude of the S feature is determined by the backaction strength, the width of this curve, remarkably, is independent of the sensor bias. Instead it reflects the thermal broadening of the reservoirs [19], indicating a constant electron temperature, independent of sensor bias V_M ; see also Appendix A 3.

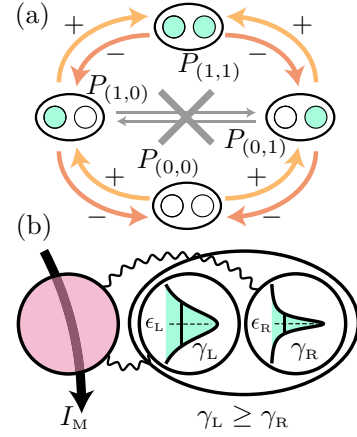


FIG. 3. Effective model. (a) Illustration of the rate equation describing the system dynamics (DD coupled to its leads). Sequential tunneling rates raise (orange arrows) or lower (red arrows) the DD's population by a single electron. Direct or virtual left-to-right charge tunneling is negligible in our system (crossed-out gray arrows) (see Appendix A). (b) The measurement backaction from the nearby charge sensor dot (pink circle) effectively imparts a different width γ_i to each dot, $i = L, R$.

III. MODEL

We develop a concise theoretical model, which provides an intuitive picture of the processes at stake, and reproduces the key features of the experiment. The open many-body dynamics of the DD system are effectively described using a rate equation, $\partial_t \mathbf{P} = \Gamma \mathbf{P}$, where \mathbf{P} is a vector containing the charge configuration probabilities, and Γ is the matrix of transition rates between the charge configurations [35, 48]. In our case, each transition between the DD charge states involves a lead to which a dot is tunnel-coupled. To lowest order, transitions between charge states of the DD occur through single electrons that hop between the DD and the leads [35]; see Fig. 3(a). We thus neglect direct $(1, 0) \leftrightarrow (0, 1)$ transitions and cotunneling between the left and right dots (see Appendix A). Hence, apparent left-to-right *switching rates* involve either the (0,0) or (1,1) as intermediates and a motion of charges in the DD necessarily involves the leads. Without detector backaction, the transition rate Γ_{if}^{\pm} from an initial (i) to a final (f) charge configuration is $\Gamma_{if}^{\pm} = \Gamma_{DD} n_f (\epsilon_f - \epsilon_i)$, where $+$ or $-$ mark raising or lowering the number of electrons in the DD, respectively. Here, we introduced the Fermi-Dirac distribution n_f , and the energies $\epsilon_{i/f}$ of the initial/final state (see Appendix B 2). We note that the Fermi-Dirac distribution of the electrons in the DD leads is the only place where the temperature enters our model.

The motion of charges through the detector capacitively modulates the energy levels in the DD. Using a quantum mechanical analysis of the transport in the system given such an out-of-equilibrium measurement, some of us have shown that the detector imparts backaction onto the DD in the form of an effective broadening of its levels [30]. Specifically, using a simple model of a quantum point contact measuring a single-level dot, high-order (coherent) energy exchange processes between the system and the detector manifested as transport

rates in the former with a Lorentzian level broadening of the dot. Crucially, our model includes direct capacitive interactions between the impinging electrons in the detector and the DD electrons, leading to distinctively different backaction signatures than those discussed in Ref. [22], where the detector is effectively described as a semiclassical phononic resonator. The Lorentzian broadening is proportional to the measurement strength and thus to V_M , which we write in our case as $\gamma_{s,L} = \alpha \chi V_M$ for the left dot and $\gamma_{s,R} = \chi V_M / \alpha$ for the right dot. The dimensionless fit parameter χ depends on the microscopic details of the detector-DD interaction [30]; see also Appendix B. Since the distance between the detector and each of the two dots is not equal, we expect the backaction-induced broadening to be different for each dot; see Fig. 3(b). We quantify this asymmetry through the parameter $\alpha = 2.2 \pm 0.2$, which we independently extract from the measurement data (see Appendix A 4). Note that the asymmetry α is necessary to enable the current through the charge sensor dot to differentiate between the left and right occupied states. Contrarily, other competing environmental effects, such as charge noise, induce an equal broadening on each level on the order of $\sim 1 \mu\text{eV}$ [49]. We include these effects through a fitting parameter ξ that encodes the (dimensionful) width and assume that the total width of the DD levels is equal to its largest contribution, such that $\gamma_j = \max(\xi, \gamma_{s,j})$ with $j = L, R$.

The level broadening γ_j modifies the system's transitions rates to $\Gamma_{if}^{\pm} = \Gamma_{DD} n_i(\epsilon_f - \epsilon_i, \gamma_j)$, where $n_i(\epsilon, \gamma)$ is a Fermi function filtered by the broadened dot level (see Appendix B 2). Using these modified rates, we compute the steady-state population imbalance Δ , and extract the maximal deviation δ_s as a function of V_M . The theoretical results in Fig. 2, are obtained with fit parameters $\chi = 9.4 \times 10^{-3}$ and $\xi = 2.5 \times 10^{-3} U$ ($\xi = 0.55 \mu\text{eV}$).

IV. PHYSICAL INTERPRETATION

The appearance of the the S-shaped charge stability diagram is a direct result of the measurement-induced imbalance α between the broadening of each dot, i.e., due to the stronger coupling between the dot closer to the sensor compared to the more distant one. To better illustrate the details of this many-body effect, we divide the transition rates as $\Gamma = \Gamma^{\text{Tail}} + \Gamma^{\text{Center}}$, where Γ^{Center} are standard thermally activated rates arising from the center of the level's spectral weight distribution; see Fig. 4. Thermal contributions to the effective broadening decrease equally for both the left and right dots as they are detuned from the chemical potential. The backaction, on the other hand, broadens the tails of the levels by a different amount for the left and right dots, leading to a more rapid reduction of the tails in the right dot when compared to the left one. In the tails (Γ^{Tail}) the backaction dominates over thermal effects, and the DD population can be controlled by the *difference* between left and right dot level broadening. Specifically, when the dot levels are far detuned from one another, or are close to the leads' chemical potentials [regions (i) and most of (ii) in Fig. 1(b)], the thermal parts dominate the rates and the tails are unimportant. Conversely, when the dots' levels are nearly degenerate and far from the chemical potentials [regions (iii) and (ii) close to the transition in Fig. 1(b)], the

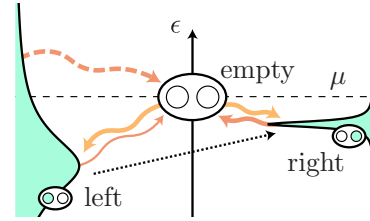


FIG. 4. Population switching due to an asymmetric detector-induced broadening. Because both levels are well below the chemical potential μ , the thermal transition rates into both levels (solid yellow arrows) are roughly equivalent. However, the thermal rates out of the quantum dots (solid orange arrows) are much larger for the right dot because its broadened level has a higher weight at the chemical potential. This imbalance, in the absence of level broadening, would lead to the left level being preferentially occupied. However, the broad tail of the left level provides an additional rate (dashed) out of the left level that causes a switch in the population; i.e., overall the probability flows from the left to right occupied state (dotted arrow). Such a configuration is found in the lower left switching region of Fig. 1(b).

tails dominate the occupation probability, leading to a switch in the population, with the high-energy state preferentially occupied; see Fig. 4.

In the literature, various detector-induced backaction mechanisms have been discussed and presented in similar double dot systems [17–24,29,32–36]. Deviations from an ideal detector performance were reported at large detector bias, where absorption of energy led to signals beyond the equilibrium setting. The majority of results discuss detector-assisted direct interdot transitions. In our work, the detector is not driven sufficiently strongly to justify direct induced transitions in the system due to energy exchange with the detector, thus differentiating our result from previous observations of backaction. This is due to the fact that the two dots are not tunnel coupled to one another; i.e., direct detector-induced transition rates (cf. Ref. [24]) are effectively zero in our experiment. This implies that our “charge-qubit flipping” transitions are induced by the detector through the interaction of the double dot with its leads. We thus base the effective model on this type of process. Note, however, that this process could have contributions due to out-of-equilibrium detector charge fluctuations that do not require quantum coherence in the detector. Nevertheless, as the fluctuations enter into the exchange between the dots and their leads, they automatically enter as a higher-order diagram, i.e., level broadening in our effective rate model. Indeed, the quenching with temperature further motivates that our backaction stems from a higher-order exchange process with the detector.

We observe clear dependence of the backaction as a function of the applied voltage in a relatively weak bias regime and are able to quench this backaction channel by increasing the temperature of the experiment. Our theoretical treatment brings forth the core of the measurement backaction effect, and remarkably, it already quantitatively reproduces the scaling behavior of the observed phenomena. Our experimental and theoretical results imply that the backaction-induced asymmetry in the level width induces the population switching. Simultaneously, we find that the type of broadening

controls the exact phase boundaries and the width of the transitions. This suggests a sharper than Lorentzian broadening, which could be due to, for example, either energy-dependent widths or higher-order charge correlations in the CSD; see Appendix B 3. Similarly, we observe particle-hole asymmetry in the S shape, which we associate to the spin of electrons on the dots; see Appendix B 4. These observations motivate further experimental and theoretical studies of such setups to better reveal the impact of the microscopic details of the detector.

V. CONCLUSIONS

Changing the nature of a many-body state simply by observing it is a major shift in how we understand and employ the act of measurement in quantum mechanics. By broadening the system's levels, the detector backaction amplifies the inevitable coupling of the quantum system with its environments, leading in turn to a complete switch in the system's electron populations. Our result goes well beyond the paradigm of ideal detectors and highlights the difficulty of keeping a system isolated yet still measurable, thus posing new challenges for quantum applications. We expect such detector-induced effects to appear in a wide variety of experimental systems, ranging from quantum dots to superconducting systems, as well as to photonic microcavities. As such, our results lay a foundation for controlling and mitigating backaction effects in future quantum technologies, e.g., by proposing limits on the allowed inbound flux of particles in the detector. Beyond applications, we open the door to the domain of many-body phases that are accessible solely due to the impact of an observer.

The data supporting this study are available in a Zenodo repository [50].

ACKNOWLEDGMENTS

We acknowledge J. D. Zimmerman and A. C. Gossard for the growth of the GaAs heterostructure. Work in Basel was supported by the Swiss Nanoscience Institute, Grant No. 179024 and NCCR SPIN of the Swiss National Science Foundation, ERC Starting Grant (D.M.Z.), and the EU H2020 European Microkelvin Platform EMP, Grant No. 824109. L.C.C. acknowledges support by Swiss NSF Mobility Fellowship No. P2BSP2 200127. C.P.S. further acknowledges support by the Georg H. Endress Foundation. The authors at ETH and IBM acknowledge financial support from the Swiss National Science Fund directly, and through NCCR QSIT. O.Z. acknowledges support from the Deutsche Forschungsgemeinschaft (DFG), Project No. 449653034.

L.C.C., D.E.F.B., C.P.S., and D.M.Z. performed the experimental work. M.S.F., C.M., B.B., and O.Z. performed the theoretical work. M.S.F., L.C.C., C.M., and O.Z. wrote the manuscript. All authors discussed the results and the manuscript.

APPENDIX A: EXPERIMENTAL SETUP

The measurements are performed in a surface-gate defined double quantum dot device fabricated on top of a GaAs

two-dimensional electron gas (2DEG) with a nominal density $n = 2.6 \times 10^{11} \text{ cm}^{-2}$ and a mobility $\mu = 4 \times 10^5 \text{ cm}^2/\text{Vs}$. The device is described in more detail in Ref. [35] and the gate layout is adapted from Ref. [51]. The device is cooled down to a base temperature of 25 mK in a $^3\text{He}/^4\text{He}$ dilution refrigerator equipped with home-built microwave filters resulting in a sample electron temperature $T_{\text{el}} \approx 65 \text{ mK}$ [52]. Applying negative voltages to surface gates allows us to locally deplete the underlying 2DEG and form two quantum dots in the center of the device; see inset of Fig. 1(a). Each quantum dot is tunnel-coupled to its respective lead with coupling rates Γ_{DD} on the order of 100 kHz (see Fig. 6), while the interdot coupling is reduced to a few Hz. For such small coupling strengths, direct (left \leftrightarrow right) tunneling and cotunneling processes through the reservoirs are strongly suppressed. We thus discard cotunneling and direct tunneling [crossed out arrows in Fig. 3(a)] as these rates are very small. We can enable direct tunneling to wash out the asymmetric effect of backaction. This is how we obtained the reference charge stability diagram of Fig. 1, where the interdot coupling washes out the backaction effect, despite a relatively large measurement bias $V_{\text{M}} = 150 \mu\text{V}$ ($0.70U/e$). Note that, in comparison to similar experiments, we generally apply a relatively small sensor bias V_{M} , and eV_{M} is well below the orbital energies of the DD and CSD.

The charge state of the double quantum dot (DD) is continuously monitored by the capacitively coupled sensor quantum dot operating as a charge sensor dot (CSD) on the left side of the device; see inset Fig. 1(a). The charge sensor bandwidth of about 15 kHz is limited by the capacitance of the low-pass microwave filters [52] on the input of the current-to-voltage converter (Basel Precision Instruments LNHS LSK389A). We tune the double dot close to the (1,0)-(0,1) charge degeneracy; see Fig. 1(a). Here, due to a low interdot tunnel-coupling compared with the coupling to the leads, a diamond-shaped region bounded by the extension of the lead-dot transitions appears, where metastable (1,0) \leftrightarrow (0,1) charge state switching occurs [35]. At each position within the diamond, the charge state switching is recorded in real time over a large number of switching events and digitized [35]. From such real-time traces, the average state-occupation probabilities (Fig. 5), as well as the switching frequency and associated transition rates (Fig. 6), are calculated from the accumulated times spent in each level [35]. We then use the real-time data to map the conductance of the CSD to the population imbalance Δ . In turn, this allows us to extract the amplitude of δ_s over a large set of parameters T, V_{M} .

The charge stability diagrams are obtained by scanning the voltage on gate V_{L} vs V_{R} ; see Fig. 5(a). Upon changing these gate voltages, a linear feedback is applied to the sensor plunger gate to compensate for capacitive crosstalk with the charge sensor. This correction bears no relevance to the effects discussed in this work and simply keeps the detector in a sensitive configuration.

Using an affine transformation

$$\begin{pmatrix} \epsilon_{\text{L}} \\ \epsilon_{\text{R}} \end{pmatrix} = \begin{pmatrix} I_{\text{LL}} & I_{\text{LR}} \\ I_{\text{RL}} & I_{\text{RR}} \end{pmatrix} \begin{pmatrix} V_{\text{L}} - V_{\text{L}}^0 \\ V_{\text{R}} - V_{\text{R}}^0 \end{pmatrix} \quad (\text{A1})$$

the two-dimensional maps in the voltages V_{L} and V_{R} are transformed into the basis of ϵ_{L} and ϵ_{R} , i.e., the energy of the left and the right quantum dot, respectively; see Fig. 5(b). The

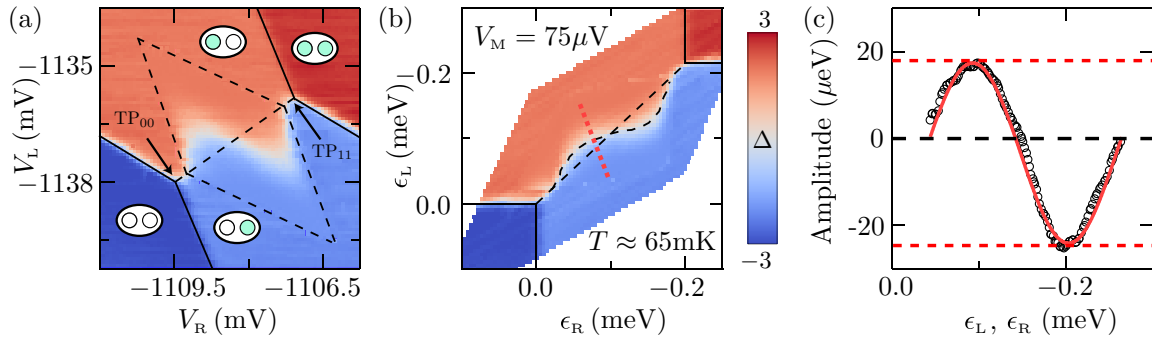


FIG. 5. Extracting the amplitude of the S shape. Measured charge state probabilities around the (1,0)-(0,1) charge degeneracy. (a) A scan as a function of the left plunger gate voltage V_L versus the voltage on the right plunger gate V_R . Probabilities inside the dashed diamond were obtained by analyzing real-time data traces of sensor conductance [35]. For the data outside the diamond, the sensor conductance was mapped to charge state configurations. The resulting occupation imbalance Δ maps are identical but the real-time measurements give more information such as the switching rate (see Fig. 6). The zero-detuning line $\epsilon_L = \epsilon_R$ is emphasized as a dashed line stretching between the triple points (TPs). The latter, labeled by TP_{00} and TP_{11} , mark degeneracy between three possible charge configurations. (b) The same data rotated into the ϵ_L - ϵ_R basis, i.e., as a function of the energy of the left and right quantum dots, respectively. As the electron has a negative charge, positive voltages correspond to negative energies. The red dotted line indicates a cut, perpendicular to the transition line, used to compute the transition widths in Fig. 8. In total for Fig. 8 we use four cuts distributed along the length of the transition line. (c) Extracted S shape where its maximal amplitude δ_s is obtained by fitting a sine model to this data (red curve). The pronounced amplitude offset is discussed in Appendix A 2.

voltage offsets V_L^0 and V_R^0 are introduced such that the triple point TP_{00} associated with the empty state occurs at $\epsilon_L = \epsilon_R = 0$. The lever arms l_{ij} have units of charge and quantify the energy shift in the $i = L, R$ level due to a change in the $j = L, R$ gate voltage. The relative magnitudes of the lever arms are found by ensuring that (i) the (1,0)-(0,1) degeneracy line lies along $\epsilon_L = \epsilon_R$, and (ii) the degeneracy lines that involve only a transition in the left (right) dot are horizontal (vertical). We calibrated the lever arm by fitting a Fermi-Dirac function to the lead transitions at elevated temperatures [23,35].

The effect of sensor-dot backaction results in a deviation of the (1,0)-(0,1) charge degeneracy line from the conventional

equilibrium phase boundary of a standard double quantum dot; see Fig. 1. To quantify this backaction effect, the energy difference between the measured and the conventionally expected (1,0)-(0,1) degeneracy line is extracted along its full extent, i.e., between the two triple points where a degeneracy occurs also with the (0,0) or the (1,1) states; see Fig. 5(c). The maximal amplitude of this deviation, δ_s , is obtained by fitting a sine model to this extracted data; see Appendix A 1. This amplitude δ_s is extracted for different biases over the sensor quantum dot and temperatures; see Fig. 2.

While not discussed in the main text, we notice a difference in the magnitude between two amplitudes of the

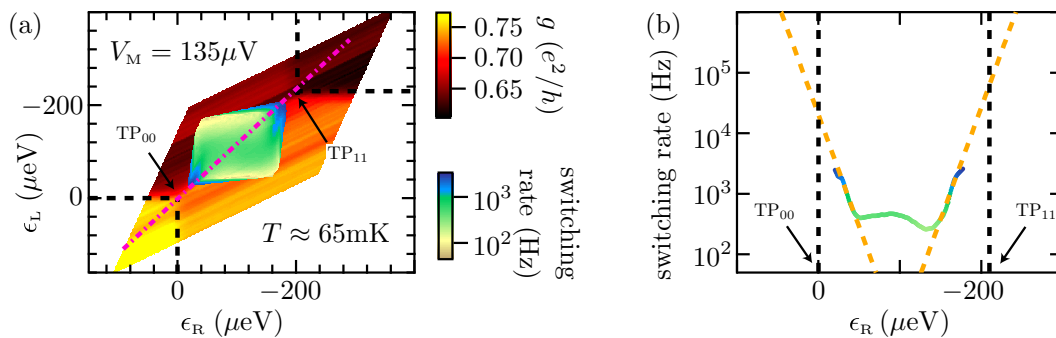


FIG. 6. Estimation of tunnel-coupling rates between the dots and their respective leads. (a) Charge stability diagram using the measured conductance through charge sensor (black-red-yellow color scale) with the four main different values corresponding to the four double dot charge states; cf. Fig. 9. The switching rate is extracted by analyzing individual real-time traces for each pixel and is overlaid on top of the conductance data (gray-green-blue color scale); see Ref. [35]. The pink dashed line indicates the cut along the zero-detuning line shown in (b). The range of switching-rate data available is limited by the finite bandwidth of the charge sensor. (b) Cut of the switching-rate map along the zero-detuning line; cf. the pink dashed line in panel (a) (gray-green-blue colored data points). To estimate the bare tunnel rate of the quantum dots Γ_{DD} , the exponential region of the switching rate is fitted and extrapolated to the triple points $TP_{0,0}$ and $TP_{1,1}$, respectively (orange dashed curves). From this fit, we estimate Γ_{DD} between 10 and 200 μ V. The saturation of the switching rate appearing between the exponential region (~ 200 to 400 μ V) is understood in terms of higher-order electron exchange effects (cotunneling) via the leads [35] and is neglected in our model as it is very small. The switching rate flattens off for the highest rates measured due to finite sensor bandwidth. This error-prone regime is ignored for the exponential fit.

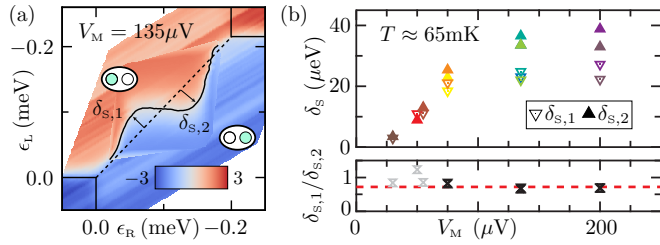


FIG. 7. Asymmetry in the backaction-induced S shape. (a) Charge stability diagram taken at a sensor bias $V_M = 135 \mu\text{V}$ which exhibits a pronounced asymmetry of the two amplitudes of the S features labeled $\delta_{s,1}$ and $\delta_{s,2}$. (b) Dependence on the sensor bias voltage V_M of the two amplitudes $\delta_{s,1}$ and $\delta_{s,2}$. Each measurement is shown with an individual color with triangles pointing upward (downward) for the amplitudes $\delta_{s,1}$ ($\delta_{s,2}$). In the lower graph, the ratio $\delta_{s,1}/\delta_{s,2}$ is shown. This ratio remains about constant with bias voltage V_M . The red dashed line indicates the calculated average ratio $(\delta_{s,1}/\delta_{s,2})_{\text{avg}} = 0.72 \pm 0.03$ for the 6 black data points. Data for $V_M < 50 \mu\text{V}$ (grayed-out markers) were excluded for the calculation of $(\delta_{s,1}/\delta_{s,2})_{\text{avg}}$ (see Appendix A 2). This asymmetry ($\delta_{s,1}/\delta_{s,2} \neq 1$) is a result of spin which breaks the particle-hole symmetry (see Appendix B 4).

S feature: the deviation of the (0,1) charge state into the conventional (1,0) region generally shows a smaller amplitude compared to the deviation into the (0,1) region; see Fig. 5(c). This asymmetry is further discussed in Appendices A 2 and B 4. There we show that the spin degeneracy of the electronic levels can explain this asymmetry. In the main text, δ_s is extracted from the amplitude of the sine fit without taking the asymmetry of the S feature into account. As a consequence, δ_s of the main text is the average of the two amplitudes.

1. Quantifying δ_s of the S shape

We extract the contour curve at which the (1,0) and (0,1) charge states have equivalent probability [dashed curve in Fig. 5(b)]. For a system without any quantum-sensor backaction, this equiprobability line coincides with the zero-detuning ($\epsilon_L = \epsilon_R$) line. Here, however, we observe a measurement-induced S-shaped deviation. In Fig. 5(c), we show a plot of the extracted difference between the zero-detuning line to the extracted S-shaped contour curve. Such plots are used to quantify the amplitudes of the S-shaped feature. We then obtain δ_s , the maximal amplitude of the S-shaped feature, by fitting the extracted data with a sine model. Note that there is an offset present in the data, due to the asymmetry of the S feature discussed in Appendix A 2, which we ignore in the main article. We obtain the error bars in δ_s in Fig. 2 by estimating the uncertainty when extracting the S feature in the occupation imbalance map: Therefore, we compare δ_s for $\Delta = 0$ (charge degeneracy) with δ_s for $\Delta = 0.2$ and $\Delta = -0.2$. This corresponds to a 10% uncertainty of the ratio $P_{(1,0)}/P_{(0,1)}$.

2. Asymmetry of the S shape

We find an asymmetry of the S shape for larger sensor-bias voltages V_M : the amplitude of the deviation from the zero-detuning line ($\epsilon_L = \epsilon_R$) closer to (0,0), labeled $\delta_{s,1}$ in Fig. 7(a), is smaller than the deviation $\delta_{s,2}$ located closer to

the (1,1) state. In Fig. 7(b), the triangles represent $\delta_{s,2}$ (filled upward triangles) and $\delta_{s,1}$ (empty downward triangles) for the individual measurements of the bias dependence. Individual measurements are presented in different colors. A clear trend is recognized in the data: a stronger quantum measurement backaction (larger sensor-bias voltage) leads to a larger absolute difference of the two amplitudes. However, the ratio $\delta_{s,1}/\delta_{s,2}$, also shown in Fig. 7(b), remains approximately constant. In the low-bias regime ($V_M < 50 \mu\text{V}$), the deviation from the zero-detuning line is small, and it is difficult to extract the amplitudes $\delta_{s,1,2}$. Therefore, the ratio $\delta_{s,1}/\delta_{s,2}$ becomes error-prone in this regime. The outlier at $V_M = 50 \mu\text{V}$ is attributed to these difficulties. For that reason, we exclude the low-bias data when calculating the average ratio $(\delta_{s,1}/\delta_{s,2})_{\text{avg}} = 0.72 \pm 0.03$ for the data with $V_M > 50 \mu\text{V}$. Note that $(\delta_{s,1}/\delta_{s,2})_{\text{avg}} \neq 1$ indicates that there is a systematic asymmetry of the S shape. As discussed in Appendix B 4, this asymmetry suggests that the particle-hole symmetry of the system is broken by the spin degree of freedom.

Note that in Fig. 2, the average values of the individual measurements of Fig. 7(b) are shown.

3. Transition width

To better understand the nature of the measurement backaction transition which we have observed, we investigate the scaling properties of the transition width. First, we extract δ_γ , the broadening of the (1,0)-(0,1) transition, by analyzing cuts through the transition in the charge stability diagram [see Fig. 5(b)]. We present an example of such a cut in Fig. 8(a). These data indicate a typical broadening in Δ of the transition from the charge state (1,0) to (0,1). To obtain δ_γ , we fit this data with a scaled Fermi-Dirac function

$$F(\epsilon, \delta_\gamma) = 4[1 + e^{(\epsilon - \lambda)/\delta_\gamma}]^{-1} - 2, \quad (\text{A2})$$

where λ is an irrelevant free parameter that shifts the distribution left or right. We then repeat this procedure for several cuts across the transition and average the result, before repeating the procedure for each charge stability diagram associated with a data point in Fig. 8.

We find no dependence of δ_γ on the sensor bias V_M as presented in Fig. 8(b), which indicates that the measurement backaction does not dominate the broadening whereas it dominates the amplitude δ_s . The data in Fig. 8(b) were obtained at a base temperature of the dilution refrigerator, corresponding to an electronic temperature $T \approx 65 \text{ mK}$ ($0.026U/k_B$). Next, we investigate the temperature dependence of δ_γ at a fixed sensor bias voltage $V_M = 75 \mu\text{V}$ ($0.35U/e$); see Fig. 8(c). When we increase the temperature, we find a linear dependence of the broadening δ_γ upon increasing the electron temperature T . Furthermore, we find that the transition width δ_γ as a function of temperature T is in good agreement with the thermal energy $\delta_\gamma \approx k_B T$ [19].

As the width shrinks linearly with diminishing temperature, the experiment is in agreement with a phase transition. A saturation of the width at lower temperatures $\delta_\gamma(T \rightarrow 0) > 0$ is still possible and would indicate the presence of an abrupt crossover, with a small but finite width [47]. The transition width is strongly tied to the nature of the tails, see

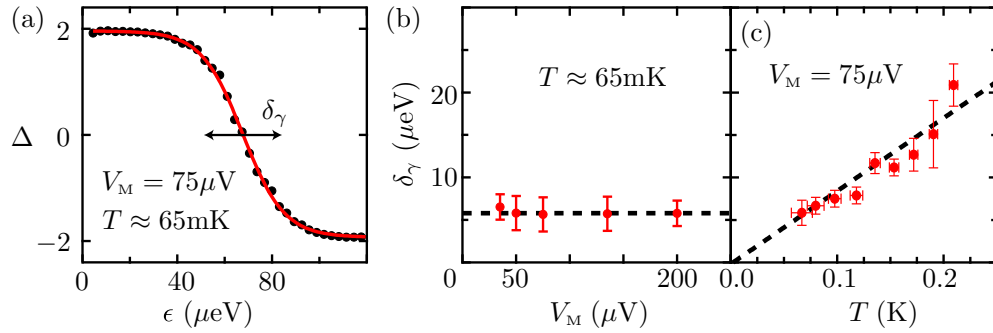


FIG. 8. Transition width. (a) Population imbalance Δ along a cut perpendicular to the (1,0)-(0,1) transition in the charge stability diagram, such as the one in Fig. 5. Here, ϵ is the Euclidean distance along the cut. We obtain the interdot transition broadening δ_γ by fitting the data to a Fermi-Dirac distribution. For each charge stability diagram, we average the width over three cuts in the energy basis (ϵ) and one cut in the voltage basis (V). (b) The width δ_γ shows no clear dependence on the sensor bias voltage V_M and, therefore, does not depend on the backaction. The dashed line indicates the thermal energy $k_B T$ associated with the electronic temperature $T = 65$ mK. (c) Temperature dependence of the width δ_γ at fixed measurement bias voltage $V_M = 75$ μ V. Over the entire temperature range in our experiments, the extracted width is similar to the thermal energy $k_B T$ (dashed black line).

Appendix B 3, motivating further studies to investigate the microscopic details of the broadening mechanism.

4. Estimation of α

We now describe the estimation of the ratio between the Coulomb interaction of sensor-to-left dot (U_{LM}) and the sensor-to-right dot (U_{RM}): $\alpha^2 = U_{LM}/U_{RM}$. Starting from an empty DD charge configuration, (0,0), the change in sensor conductance g_Δ when adding an electron to the left dot $|g^{(0,0)} - g^{(1,0)}|$ is different from that observed when adding an electron to the right dot $|g^{(0,0)} - g^{(0,1)}|$. Under the assumption that, in the region of interest, the sensor conductance is linear in sensor quantum dot energy, we obtain an approximation of α by comparing the magnitudes of g_Δ for different charge transitions; see Fig. 9.

Generally, we observe four main values of conductance g through the charge sensor, corresponding to the four relevant charge configurations of the DD. This is demonstrated in Fig. 9: here a histogram of the charge sensor signal for a charge stability diagram around the (1,0)-(0,1) double

dot transition is presented. From the specific data shown in Fig. 9, we obtain $\alpha^2 = U_{LM}/U_{RM} \approx (g^{(0,0)} - g^{(1,0)})/(g^{(0,0)} - g^{(0,1)}) = 5.4$. Repeating the process for several distinct experimental parameters we obtain an estimate $\alpha = 2.2 \pm 0.2$ which we use in the theoretical model.

APPENDIX B: MODEL

1. Microscopic model

The full microscopic model describing the system-detector setup can be written using the Hamiltonian

$$H = H_{\text{DD}} + H_{\text{leads}} + H_{\text{tun}} + H_M + H_{\text{int}}, \quad (\text{B1})$$

including the double quantum dot H_{DD} , its leads H_{leads} , tunnel-coupling between the dots and their respective leads H_{tun} , the detector model H_M , and the system-detector interaction H_{int} terms. The double dot Hamiltonian $H_{\text{DD}} = H_L + H_R + H_{\text{coupl}}$ is in turn described by the Hamiltonians H_L and H_R of the left and right dots, and a coupling Hamiltonian H_{coupl} . Assuming at most a single orbital mode in each of the dots

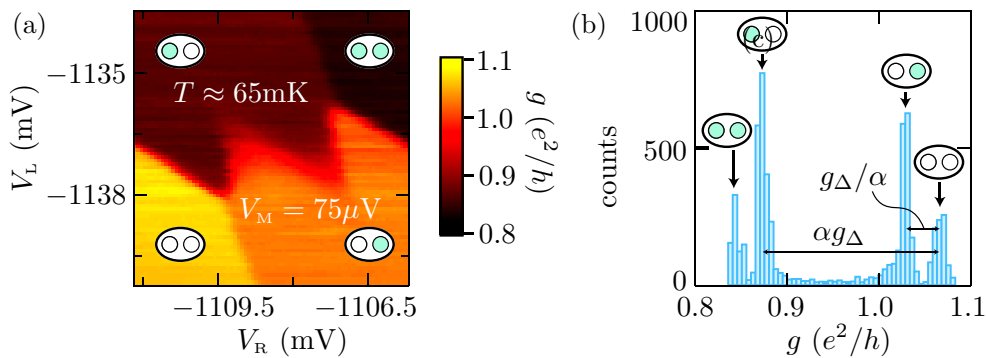


FIG. 9. Measuring the asymmetry α of the level widths. (a) Sensor conductance g of the charge stability diagram around the (1,0)-(0,1) charge state configurations of the double dot. Due to different capacitive coupling of the DD to the charge sensor, the four charge states are distinguishable by their characteristic sensor conductances. (b) Histogram of the charge stability diagram shown in (a). Each charge state in panel (a) appears at different but roughly constant sensor conductance which results in peaks when plotted as a histogram. The parameter α is estimated by the ratio of the difference g_Δ in conductance g of the charge states involved.

and in the absence of magnetic field, we write the left dot Hamiltonian as

$$H_L = \sum_{\sigma} \epsilon_L d_{L\sigma}^{\dagger} d_{L\sigma} + U_L d_{L\uparrow}^{\dagger} d_{L\uparrow} d_{L\downarrow}^{\dagger} d_{L\downarrow}, \quad (\text{B2})$$

where $d_{L\sigma}^{\dagger}$ ($d_{L\sigma}$) creates (annihilates) an electron with spin σ and energy ϵ_L in the left dot. The on-site Coulomb repulsion U_L , which is on the order of a few meV, is much larger than all relevant energy scales in the system such that the doubly occupied state of the left dot is energetically forbidden. Due to the absence of magnetic field the two spin states are degenerate, such that in our analysis the difference between including and excluding spin is the inclusion of a degeneracy factor; see Appendix B 4. The right dot Hamiltonian is obtained in an analogous way to H_L but with the substitution $L \rightarrow R$. In the following we drop the spin degree of freedom and associated index σ for simplicity. The left and right dot Hamiltonians then become

$$H_i = \epsilon_i d_i^{\dagger} d_i \quad (\text{B3})$$

for the left $i = L$ and right $i = R$ dots. The two dots are only electrostatically coupled, as the tunneling barrier between them is very large, such that the coupling Hamiltonian becomes

$$H_{\text{coupl}} = U d_L^{\dagger} d_L d_R^{\dagger} d_R, \quad (\text{B4})$$

where the mutual charging energy (experimentally estimated $U \approx 215 \mu\text{eV}$) penalizes the simultaneous occupancy of the left and right dots. The total double dot Hamiltonian is thus

$$H_{\text{DD}} = \epsilon_L d_L^{\dagger} d_L + \epsilon_R d_R^{\dagger} d_R + U d_L^{\dagger} d_L d_R^{\dagger} d_R, \quad (\text{B5})$$

which has the empty, left-, right-, and doubly occupied states as eigenstates.

The left and right leads are described by

$$H_{\text{leads}} = \sum_{k, i=L, R} \epsilon_{ik} c_{ik}^{\dagger} c_{ik}, \quad (\text{B6})$$

where k indexes the different momenta of the leads and c_{ik}^{\dagger} (c_{ik}) creates (annihilates) an electron with energy ϵ_{ik} in the left $i = L$ or right $i = R$ leads. Each of these leads is further associated with a tunable chemical potential $\mu_{L, R}$, which is kept constant and at equilibrium, serving as the energy reference for the experiment, $\mu_L = \mu_R = 0$. This is described by the tunneling Hamiltonian

$$H_{\text{tun}} = \sum_{k, i=L, R} t (d_i^{\dagger} c_{ik} + \text{H.c.}), \quad (\text{B7})$$

where the tunneling amplitude t is taken to be momentum independent and equal for both dots, as is the case in the experiment.

The detector Hamiltonian is built up in a similar fashion but with a single dot

$$H_M = \epsilon_M d_M^{\dagger} d_M + \sum_{k, i=s, d} [\epsilon_{ik} c_{ik}^{\dagger} c_{ik} + t_M (d_M^{\dagger} c_{ik} + \text{H.c.})]. \quad (\text{B8})$$

Here all quantities are defined analogously to the double dot and its leads, but with new indices for the detector dot (M), as well as for the source (s) and the drain (d) detector leads. A bias voltage across the detector V_M is directly proportional

to the difference between source and drain chemical potential $\mu_{\text{sd}} = \mu_s - \mu_d$. Finally, the interaction Hamiltonian describes capacitive coupling between the measurement dot and both the left and right dots:

$$H_{\text{int}} = (U_{\text{LM}} d_L^{\dagger} d_L + U_{\text{RM}} d_R^{\dagger} d_R) d_M^{\dagger} d_M. \quad (\text{B9})$$

Here, we introduced the two Coulomb interaction strengths U_{LM} and U_{RM} between the left or right dot and the measurement dot. Essential to our work, these interaction terms are not equal due to the different distances between the detector and the two dots. We define their ratio as

$$\alpha^2 = U_{\text{LM}}/U_{\text{RM}}. \quad (\text{B10})$$

As shown in Appendix A 4, this value is experimentally determined to be $\alpha = 2.2 \pm 0.2$.

2. Rate equation with backaction

We analyze transport through the DD using a rate equation. To this end, we assume a sufficiently small tunnel coupling between the dots and their leads $\rho_i |t|^2 \ll U$ with ρ_i the density of states of lead i . We then perturbatively derive the corresponding sequential tunneling rates using Fermi's golden rule [48]. In the absence of the detector, Fermi's golden rule for the symmetrically coupled DD reads [35]

$$\Gamma_{if} = \Gamma_{\text{DD}} \int d\epsilon \delta(\epsilon - \epsilon_i + \epsilon_f) n_F(\epsilon) = \Gamma_{\text{DD}} n_F(\epsilon_f - \epsilon_i), \quad (\text{B11})$$

where i, f denote initial and final states [described by different charge configurations (N_L, N_R) of the DD], $\Gamma_{\text{DD}} = 2\pi \rho |t|^2 / \hbar$ is the bare tunneling rate with $\rho_i = \rho$, and we introduced the Fermi-Dirac distribution

$$n_F(\epsilon) = \frac{1}{1 + \exp(\epsilon/k_B T)}. \quad (\text{B12})$$

One of the central results of Ref. [30] is that, when calculating such transport rates through the system, a continuous charge measurement of a quantum dot enters as an effective width for the dot's energy level. Using this result, we effectively trace out the detector and incorporate its impact directly in a slightly modified expression for the rates

$$\Gamma_{if} = \Gamma_{\text{DD}} \int d\epsilon \frac{1}{\pi} \frac{\gamma_{f-i}}{\epsilon^2 + \gamma_{f-i}^2} n_F(\epsilon_f - \epsilon_i + \epsilon), \quad (\text{B13})$$

where the width γ_{f-i} depends on the relevant dot level associated to the specific rate. For example, if $f = (1, 1)$ and $i = (1, 0)$ then $\gamma_{f-i} = \gamma_R$ because only the right dot is involved in the tunneling process. Performing the integral we obtain

$$\Gamma_{if} = \Gamma_{\text{DD}} n_L(\epsilon_f - \epsilon_i, \gamma_{f-i}), \quad (\text{B14})$$

where we have introduced the modified Fermi-Dirac distribution

$$n_L(\epsilon, \gamma) = \frac{1}{2} + \text{Im} \psi \left(\frac{1}{2} + \frac{\gamma - i\epsilon}{2\pi k_B T} \right), \quad (\text{B15})$$

and ψ is the digamma function. These rates have algebraic tails which decay as $\sim \gamma/\epsilon$ for large ϵ [48]. We use this phenomenological approach motivated by previous works [30,31], and leave more detailed calculations for future work.

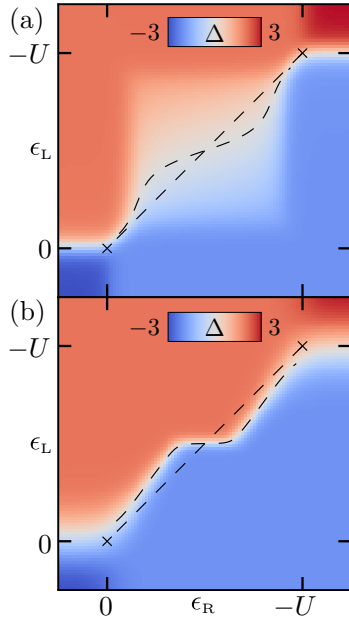


FIG. 10. Theoretically calculated imbalance Δ using the rate equation, while including the effect of measurement backaction. We use the same parameters as in the experimental plot Fig. 1(b). The measurement bias is $V_M = 0.35U$, the temperature is $T = 0.026U/k_B$, and the asymmetry in the coupling is $\alpha = 2.2$. (a) Using the Lorentzian broadening (B14) of the DD due to backaction, with the fit parameters $\chi = 9.4 \times 10^{-3}$ and $\xi = 2.5 \times 10^{-3}U$. (b) Using a Gaussian broadening (B17) of the DD due to backaction, with the fit parameters $\chi^G = 0.099$ and $\xi^G = 0.084U$. We notice that the shape of the anomaly is more similar to the experiment in the Lorentzian case, while the width of the transition is better captured by the Gaussian approach. Here, the Gaussian broadening is merely used as a sufficiently distinct counterexample to the Lorentzian broadening but is not suggested by any theory.

We substitute the rates (B14) into a rate equation, describing the time evolution of the occupation probability of each charge state i ,

$$\partial_t P_i = \sum_j P_j \Gamma_{ij} - P_i \sum_j \Gamma_{ij}, \quad (\text{B16})$$

leading to a Markovian chain as illustrated in Fig. 3(a). Solving for the steady state $\partial_t P_i = 0$, we obtain the mean/observable charge states of the DD and thus the imbalance Δ ; see Fig. 10. We can then extract δ_s from these charge stability diagrams and use the result to fit χ and ξ ; see Fig. 2.

3. Nature of the tails

In Ref. [30], backaction was predicted to cause a Lorentzian broadening of the delta function in Fermi's golden rule (B11), leading to the broadened rates (B14). Here, we point out that the shape of the tails has a strong influence on the exact form of the population-switching region, or S shape, and the width of the transition. We use a Gaussian widening of the level as a counterweight to the Lorentzian ones. While there are no works suggesting such a broadening, it is useful as an extreme example, completely opposed to the Lorentzian. Here, we look at the not physically motivated Gaussian broad-

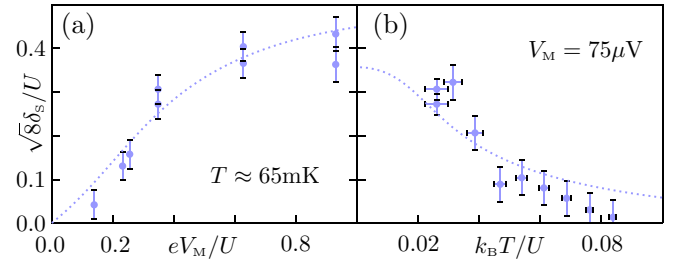


FIG. 11. Fitting the imbalance with Gaussian broadenings. Measured maximal deviation δ_s (circles) as a function of the measurement bias voltage V_M (a) and temperature T (b) as in Fig. 2. A Gaussian broadening of the levels leads to a qualitatively similar scaling (dotted line) of the maximal deviation δ_s as both the experiment and the Lorentzian broadening; cf. Fig. 2. Unlike the Lorentzian broadening, there is no clear saturation for a given α in the case of Gaussian broadening.

ening to conclude that our Lorentzian-broadening model is incomplete.

These distributions have very different properties, which manifest in the shape and contrast of the charge stability diagrams; see Fig. 10. However, the qualitative behavior of the population switching and the scalings with temperature and bias remain the same; see Fig. 11. This motivates future work, which will investigate the nature of the population-switching transition at low temperatures, to determine among other things whether this is a phase transition or abrupt crossover. A likely contribution to the specific shapes is also that the Lorentzian widths γ may in general depend on the parameters ϵ_L , ϵ_R , T of the system.

To include a Gaussian width we replace the delta function δ in the rate calculation (B11) through

$$\delta(\epsilon - \epsilon_i + \epsilon_f) \rightarrow \frac{1}{\sqrt{\pi} \gamma_{f-i}} \exp \left[\frac{-(\epsilon - \epsilon_i + \epsilon_f)^2}{\gamma_{f-i}^2} \right], \quad (\text{B17})$$

and then evaluate the integral numerically. Recall that γ_{f-i} is either γ_L^G or γ_R^G depending on which level is involved in the transition $i \rightarrow f$ (we use G to indicate parameters that belong to the Gaussian model). We can then use the rate equation (B16) to compute the steady state by imposing $\partial_t P = 0$, for both the Lorentzian and Gaussian broadenings; see Fig. 10. From there, we extract a width δ_s for a given set of fitting parameters χ , ξ and the experimental parameters V_M , T , and α . In the main text, for the Lorentzian we used only the largest of the background or bias induced widths $\gamma_j = \max(\xi, \gamma_{s,j})$, which is functionally similar to root square addition $\gamma_j = \sqrt{\xi^2 + \gamma_{s,j}^2}$ of the widths, which is typical of Lorentzian line broadening. However such an approach to the Gaussian widths cannot be expected to capture the experimentally observed signatures. Specifically, the growth of one of the widths while the other remains constant causes the rapid formation of a very large δ_s , due to the rapid decay in the tails of the Gaussian. Instead of simply using the larger of the two rates, we therefore add the two contributions linearly for the Gaussian, such that

$$\gamma_j^G = \xi^G + \gamma_{s,j}^G, \quad (\text{B18})$$

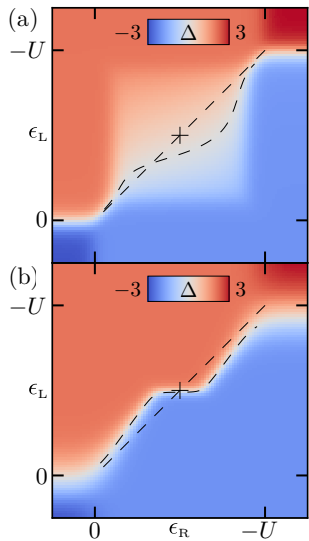


FIG. 12. Effect of spin. A theoretical prediction for the S shape for a model with spin-degenerate levels, for both Lorentzian (a) and Gaussian (b) broadenings. In the Lorentzian case we notice a significant particle-hole symmetry breaking, while in the Gaussian case it is barely visible (distance between the S shape and the black cross). Parameters as in Fig. 10, except for the inclusion of spin; see Eq. (B19).

where $\gamma_{s,L}^G = \alpha \chi^G V_M$ and $\gamma_{s,L}^G = \chi^G V_M / \alpha$. Of course a microscopic investigation of the exact nature of the tails must also provide a prescriptive way of adding the widths. Here, however, we aim to qualitatively understand the physical processes at stake and thus leave these details to future works. We calculate the imbalance Δ as a function of T and V_M to fit $\chi^G = 0.099$ and $\xi^G = 0.084U$; see Fig. 11. Note that the resulting value for ξ is nearly an order of magnitude larger than the expected value $\sim 1 \mu\text{eV}$ [49].

In a typical experimentally relevant situation, cf. Fig. 1(b) and Fig. 10, we notice that the shape of the S feature is better captured by the Lorentzian broadening, while the width is better described by the Gaussian. We conclude that the precise form of the broadening can be investigated using the complete charge stability diagrams. While our brief description here suggests an intermediate *between* a Lorentzian and a Gaussian, this can be achieved in a multitude of ways, e.g., parameter (ϵ) dependent broadenings (γ) or different power

law decays. Furthermore, as (part of) the CSD level lies in the measurement bias window we expect resonant effects, which must be resummed to be accounted for properly. The dependence of region (iii) in Fig. 1(b) on these effects will be the focus of future studies.

4. Asymmetry in the S shape

As discussed in Appendix A 2, the experimental data show an asymmetry in the S shape, which breaks the particle-hole symmetry of the $\epsilon_L = -U/2$, $\epsilon_R = -U/2$ configuration. If both left and right levels are allowed to be spin degenerate (as expected in the zero magnetic field experiment) this leads to overall degeneracies of 1,2,2,4 for the empty, left-, right-, and doubly occupied states, respectively. The fact that the empty and doubly occupied states have different degeneracies manifestly breaks particle-hole symmetry. We conclude that spin degeneracy is a candidate for the asymmetry seen in the experiment. To further investigate this property, we include the degeneracies in our rate equation, which leads to a transformation

$$\Gamma^+ \rightarrow 2\Gamma^+, \quad \Gamma^- \rightarrow \Gamma^-, \quad (\text{B19})$$

in the rates which add or remove electrons from the DD.

The result of performing this substitution is very different in the case of Lorentzian broadening when compared to Gaussian broadening; see Figs. 12(a) and 12(b), respectively. In the latter case, the decay of the rates as a function of ϵ_L and ϵ_R is exponential. Thus as the widths are relatively small the factor of two in the rates causes only a small shift in the intersection between the diagonal and the S shape. On the other hand, the tails of the Lorentzian are algebraic and do not, therefore, have a characteristic scale on which they decay. The intersection between the diagonal and the S shape can thus shift significantly even for small broadenings. This shift leads to a bias-dependent asymmetry of the S-shape amplitudes $\delta_{s,1}$ and $\delta_{s,2}$ as observed in the experiment; see Fig. 7.

We conclude that spin is a likely candidate for the experimentally observed particle-hole asymmetry; see Appendix A 2. Furthermore, the very large (small) asymmetry in the Lorentzian (Gaussian) case compared to the experimental evidence in Fig. 7 again indicates that the broadening is sharper than Lorentzian. This strong dependence of the asymmetry on the type of tails, see Fig. 12, shows that it can be used as a signature to investigate the precise nature of the tails.

- [1] M. A. Nielsen and I. L. Chuang, *Quantum Computation and Quantum Information: 10th Anniversary Edition* (Cambridge University Press, Cambridge, United Kingdom, 2011).
- [2] J. J. Pla, K. Y. Tan, J. P. Dehollain, W. H. Lim, J. J. L. Morton, F. A. Zwanenburg, D. N. Jamieson, A. S. Dzurak, and A. Morello, High-fidelity readout and control of a nuclear spin qubit in silicon, *Nature (London)* **496**, 334 (2013).
- [3] D. M. Zajac, A. J. Sigillito, M. Russ, F. Borjans, J. M. Taylor, G. Burkard, and J. R. Petta, Resonantly driven CNOT gate for electron spins, *Science* **359**, 439 (2018).

- [4] F. N. Froning, L. C. Camenzind, O. A. van der Molen, A. Li, E. P. Bakkers, D. M. Zumbühl, and F. R. Braakman, Ultrafast hole spin qubit with gate-tunable spin-orbit switch functionality, *Nat. Nanotechnol.* **16**, 308 (2021).
- [5] L. C. Camenzind, S. Geyer, A. Fuhrer, R. J. Warburton, D. M. Zumbühl, and A. V. Kuhlmann, A hole spin qubit in a fin field-effect transistor above 4 kelvin, *Nat. Electron.* **5**, 178 (2022).
- [6] D. Kim, D. R. Ward, C. B. Simmons, J. K. Gamble, R. Blume-Kohout, E. Nielsen, D. E. Savage, M. G. Lagally, M. Friesen, S. N. Coppersmith, and M. A. Eriksson, Microwave-driven

- coherent operation of a semiconductor quantum dot charge qubit, *Nat. Nanotechnol.* **10**, 243 (2015).
- [7] A. Wallraff, D. I. Schuster, A. Blais, L. Frunzio, R.-S. Huang, J. Majer, S. Kumar, S. M. Girvin, and R. J. Schoelkopf, Strong coupling of a single photon to a superconducting qubit using circuit quantum electrodynamics, *Nature (London)* **431**, 162 (2004).
- [8] P. Krantz, M. Kjaergaard, F. Yan, T. P. Orlando, S. Gustavsson, and W. D. Oliver, A Quantum Engineer's Guide to Superconducting Qubits, *Appl. Phys. Rev.* **6**, 021318 (2019).
- [9] D. Kielpinski, C. Monroe, and D. J. Wineland, Architecture for a large-scale ion-trap quantum computer, *Nature (London)* **417**, 709 (2002).
- [10] J. P. Home, D. Hanneke, J. D. Jost, J. M. Amini, D. Leibfried, and D. J. Wineland, Complete Methods Set for Scalable Ion Trap Quantum Information Processing, *Science* **325**, 1227 (2009).
- [11] D. Aasen, M. Hell, R. V. Mishmash, A. Higginbotham, J. Danon, M. Leijnse, T. S. Jespersen, J. A. Folk, C. M. Marcus, K. Flensberg, and J. Alicea, Milestones toward Majorana-Based Quantum Computing, *Phys. Rev. X* **6**, 031016 (2016).
- [12] H. M. Wiseman and G. J. Milburn, *Quantum Measurement and Control* (Cambridge University Press, Cambridge, United Kingdom, 2009).
- [13] A. A. Clerk, M. H. Devoret, S. M. Girvin, F. Marquardt, and R. J. Schoelkopf, Introduction to quantum noise, measurement, and amplification, *Rev. Mod. Phys.* **82**, 1155 (2010).
- [14] J. von Neumann, *Mathematische Grundlagen der Quantenmechanik* (Springer, Berlin, 1932).
- [15] S. A. Gurvitz and Y. S. Prager, Microscopic derivation of rate equations for quantum transport, *Phys. Rev. B* **53**, 15932 (1996).
- [16] A. N. Korotkov and D. V. Averin, Continuous weak measurement of quantum coherent oscillations, *Phys. Rev. B* **64**, 165310 (2001).
- [17] M. Field, C. G. Smith, M. Pepper, D. A. Ritchie, J. E. F. Frost, G. A. C. Jones, and D. G. Hasko, Measurements of Coulomb Blockade with a Noninvasive Voltage Probe, *Phys. Rev. Lett.* **70**, 1311 (1993).
- [18] J. M. Elzerman, R. Hanson, J. S. Greidanus, L. H. Willems van Beveren, S. De Franceschi, L. M. K. Vandersypen, S. Tarucha, and L. P. Kouwenhoven, Few-electron quantum dot circuit with integrated charge read out, *Phys. Rev. B* **67**, 161308(R) (2003).
- [19] L. DiCarlo, H. J. Lynch, A. C. Johnson, L. I. Childress, K. Crockett, C. M. Marcus, M. P. Hanson, and A. C. Gossard, Differential Charge Sensing and Charge Delocalization in a Tunable Double Quantum Dot, *Phys. Rev. Lett.* **92**, 226801 (2004).
- [20] D. Harbusch, D. Taubert, H. P. Tranitz, W. Wegscheider, and S. Ludwig, Phonon-Mediated versus Coulombic Backaction in Quantum Dot Circuits, *Phys. Rev. Lett.* **104**, 196801 (2010).
- [21] S. Gasparinetti, M. J. Martínez-Pérez, S. de Franceschi, J. P. Pekola, and F. Giazotto, Nongalvanic thermometry for ultracold two-dimensional electron domains, *Appl. Phys. Lett.* **100**, 253502 (2012).
- [22] G. Granger, D. Taubert, C. E. Young, L. Gaudreau, A. Kam, S. A. Studenikin, P. Zawadzki, D. Harbusch, D. Schuh, W. Wegscheider, Z. R. Wasilewski, A. A. Clerk, S. Ludwig, and A. S. Sachrajda, Quantum interference and phonon-mediated back-action in lateral quantum-dot circuits, *Nat. Phys.* **8**, 522 (2012).
- [23] D. Maradan, L. Casparis, T.-M. Liu, D. E. F. Biesinger, C. P. Scheller, D. M. Zumbühl, J. D. Zimmerman, and A. C. Gossard, GaAs quantum dot thermometry using direct transport and charge sensing, *J. Low Temp. Phys.* **175**, 784 (2014).
- [24] C. E. Young and A. A. Clerk, Inelastic Backaction due to Quantum Point Contact Charge Fluctuations, *Phys. Rev. Lett.* **104**, 186803 (2010).
- [25] Y. Aharonov, D. Z. Albert, and L. Vaidman, How the Result of a Measurement of a Component of the Spin of a Spin-1/2 Particle Can Turn Out to Be 100, *Phys. Rev. Lett.* **60**, 1351 (1988).
- [26] A. N. Korotkov, Selective quantum evolution of a qubit state due to continuous measurement, *Phys. Rev. B* **63**, 115403 (2001).
- [27] O. Hosten and P. Kwiat, Observation of the spin Hall effect of light via weak measurements, *Science* **319**, 787 (2008).
- [28] O. Zilberberg, A. Romito, D. J. Starling, G. A. Howland, C. J. Broadbent, J. C. Howell, and Y. Gefen, Null Values and Quantum State Discrimination, *Phys. Rev. Lett.* **110**, 170405 (2013).
- [29] I. Snyman and Y. V. Nazarov, Polarization of a Charge Qubit Strongly Coupled to a Voltage-Driven Quantum Point Contact, *Phys. Rev. Lett.* **99**, 096802 (2007).
- [30] O. Zilberberg, A. Carmi, and A. Romito, Measuring cotunneling in its wake, *Phys. Rev. B* **90**, 205413 (2014).
- [31] D. Bischoff, M. Eich, O. Zilberberg, C. Rössler, T. Ihn, and K. Ensslin, Measurement back-action in stacked graphene quantum dots, *Nano Lett.* **15**, 6003 (2015).
- [32] E. Onac, F. Balestro, L. H. Willems van Beveren, U. Hartmann, Y. V. Nazarov, and L. Kouwenhoven, Using a Quantum Dot as a High-Frequency Shot Noise Detector, *Phys. Rev. Lett.* **96**, 176601 (2006).
- [33] D. Taubert, M. Pioro-Ladrière, D. Schröer, D. Harbusch, A. S. Sachrajda, and S. Ludwig, Telegraph Noise in Coupled Quantum Dot Circuits Induced by a Quantum Point Contact, *Phys. Rev. Lett.* **100**, 176805 (2008).
- [34] U. Gasser, S. Gustavsson, B. Küng, K. Ensslin, T. Ihn, D. C. Driscoll, and A. C. Gossard, Statistical electron excitation in a double quantum dot induced by two independent quantum point contacts, *Phys. Rev. B* **79**, 035303 (2009).
- [35] D. E. F. Biesinger, C. P. Scheller, B. Braunecker, J. Zimmerman, A. C. Gossard, and D. M. Zumbühl, Intrinsic Metastabilities in the Charge Configuration of a Double Quantum Dot, *Phys. Rev. Lett.* **115**, 106804 (2015).
- [36] K. Horibe, T. Kodera, and S. Oda, Back-action-induced excitation of electrons in a silicon quantum dot with a single-electron transistor charge sensor, *Appl. Phys. Lett.* **106**, 053119 (2015).
- [37] M. Soriente, T. Donner, R. Chitra, and O. Zilberberg, Dissipation-Induced Anomalous Multicritical Phenomena, *Phys. Rev. Lett.* **120**, 183603 (2018).
- [38] S. Matern, D. Loss, J. Klinovaja, and B. Braunecker, Coherent backaction between spins and an electronic bath: Non-Markovian dynamics and low-temperature quantum thermodynamic electron cooling, *Phys. Rev. B* **100**, 134308 (2019).
- [39] A. J. Leggett, S. Chakravarty, A. T. Dorsey, M. P. A. Fisher, A. Garg, and W. Zwerger, Dynamics of the dissipative two-state system, *Rev. Mod. Phys.* **59**, 1 (1987).
- [40] A. Štrkalj, M. S. Ferguson, T. M. R. Wolf, I. Levkivskyi, and O. Zilberberg, Tunneling into a Finite Luttinger Liquid Coupled to Noisy Capacitive Leads, *Phys. Rev. Lett.* **122**, 126802 (2019).

- [41] A. Khedri, A. Štrkalj, A. Chiochetta, and O. Zilberberg, Luttinger liquid coupled to ohmic-class environments, *Phys. Rev. Res.* **3**, L032013 (2021).
- [42] A. Khedri, D. Horn, and O. Zilberberg, Fate of exceptional points in the presence of nonlinearities, [arXiv:2208.11205](https://arxiv.org/abs/2208.11205).
- [43] R. Hab-arrih, A. Jellal, D. Stefanatos, and A. Merdaci, Instability of Meissner differential equation and its relation with photon excitations and entanglement in a system of coupled quantum oscillators, *Quantum Rep.* **3**, 684 (2021).
- [44] S. Diehl, A. Tomadin, A. Micheli, R. Fazio, and P. Zoller, Dynamical Phase Transitions and Instabilities in Open Atomic Many-Body Systems, *Phys. Rev. Lett.* **105**, 015702 (2010).
- [45] S. Diehl, E. Rico, M. A. Baranov, and P. Zoller, Topology by dissipation in atomic quantum wires, *Nat. Phys.* **7**, 971 (2011).
- [46] K. Snizhko, P. Kumar, N. Rao, and Y. Gefen, Weak-Measurement-Induced Asymmetric Dephasing: Manifestation of Intrinsic Measurement Chirality, *Phys. Rev. Lett.* **127**, 170401 (2021).
- [47] M. Goldstein, R. Berkovits, and Y. Gefen, Population Switching and Charge Sensing in Quantum Dots: A Case for a Quantum Phase Transition, *Phys. Rev. Lett.* **104**, 226805 (2010).
- [48] H. Bruus and K. Flensberg, *Many-Body Quantum Theory in Condensed Matter Physics* (Oxford University Press, Oxford, 2004).
- [49] L. C. Camenzind, L. Yu, P. Stano, J. D. Zimmerman, A. C. Gossard, D. Loss, and D. M. Zumbühl, Hyperfine-phonon spin relaxation in a single-electron GaAs quantum dot, *Nat. Commun.* **9**, 3454 (2018).
- [50] M. S. Ferguson, L. C. Camenzind, C. Müller, D. E. F. Biesinger, C. P. Scheller, B. Braunecker, D. M. Zumbühl, and O. Zilberberg, Supporting data for “Measurement-induced population switching”, Zenodo, <https://doi.org/10.5281/zenodo.4061986>.
- [51] C. Barthel, D. J. Reilly, C. M. Marcus, M. P. Hanson, and A. C. Gossard, Rapid Single-Shot Measurement of a Singlet-Triplet Qubit, *Phys. Rev. Lett.* **103**, 160503 (2009).
- [52] C. P. Scheller, S. Heizmann, K. Bedner, D. Giss, M. Meschke, D. M. Zumbühl, J. D. Zimmerman, and A. C. Gossard, Silver-epoxy microwave filters and thermalizers for millikelvin experiments, *Appl. Phys. Lett.* **104**, 211106 (2014).